

Re-laminarization of elastic turbulence

M. Vijay Kumar^{1,2,3*}, Atul Varshney^{1,4,5*}, Dongyang Li^{1,6}, and Victor Steinberg^{1,2}

¹*Department of Physics of Complex Systems, Weizmann Institute of Science, Rehovot, Israel 76100*

²*The Racah Institute of Physics, Hebrew University of Jerusalem, Jerusalem 91904, Israel*

³*Department of Mechanical and Industrial Engineering,
University of Illinois at Chicago, Illinois 60607, USA*

⁴*School of Physical Sciences, National Institute of Science Education and Research, HBNI, Jatni-752050, Odisha, India*

⁵*Institute of Science and Technology Austria, Am Campus 1, 3400 Klosterneuburg, Austria*

⁶*College of Nuclear Science and Technology, Harbin Engineering University, Harbin 150001, China*

We report frictional drag reduction and a complete flow re-laminarization of elastic turbulence (ET) at vanishing inertia in a viscoelastic channel flow past an obstacle. We show that intensity of observed elastic waves and wall-normal vorticity correlate well with the measured drag above the ET onset. Moreover, we find that the elastic wave frequency grows with Weissenberg number, and at sufficiently high frequency it causes decay of the elastic waves, resulting in ET attenuation and drag reduction. Thus, this allows us to substantiate a physical mechanism, involving interaction of elastic waves with wall-normal vorticity fluctuations, leading to the drag reduction and re-laminarization phenomena at low Reynolds number.

Curvilinear flows of dilute polymer solution exhibit elastic instabilities and elastic turbulence (ET) at vanishing inertia. In such flows, the elastic stress generated by polymer stretching along curved streamlines initiates a back-reaction on the flow in the curvature direction and triggers a linear normal mode elastic instability and ET at $Wi \gg 1$ and $Re \ll 1$ [1, 2]. However, this instability mechanism becomes ineffective in zero curvature parallel shear flows, such as pipe, channel and plane Couette [1–6]. Here, the degree of polymer stretching [7] is defined by the Weissenberg number $Wi = \lambda U/d$ and the ratio of inertial and viscous stresses by the Reynolds number $Re = \rho U d/\eta$; U is the mean fluid speed, λ is the longest polymer relaxation time, η and ρ are the solution viscosity and density, respectively, and d is the characteristic vessel size.

The first signature of a linear elastic instability was reported in a viscoelastic channel flow obstructed by two widely spaced obstacles [6]. The linear Hopf instability occurs due to a breaking of time-reversal symmetry leading to span-wise oscillations of a pair of eddies. Further, two shear (mixing) layers with zero curvature streamlines are generated due to the vortex pair elongation with Wi [8]. It follows by a secondary transition directly to ET and elastic waves at $Re \ll 1$ [8–10]. The measured friction factor, f/f_{lam} , as a function of Wi exhibits distinct scaling exponents in three flow regimes: $Wi^{0.5}$ (transition), $Wi^{0.2}$ (ET) and $Wi^{-0.2}$ (drag reduction; DR) [6, 8, 9]. Here, f_{lam} is the friction factor for laminar flow. Remarkably, the extent of DR was reduced either with decreasing fluid elasticity $El(=Wi/Re)$ or increasing inertia (or Re), and flow re-laminarization was found at $El \geq 1000$ and $Re < 10$ [9]. It should be emphasized that both elastic waves and DR down to re-laminarization were observed only in a viscoelastic channel flow in ET [9–11].

On the other hand, an addition of minute amount of long-chain flexible polymers into high-Re shear flows causes a suppression of small-scale turbulent structures

and reduces frictional drag up to 80%, known as turbulent drag reduction (TDR) phenomenon [12]. Here, both the inertia and elastic stresses, and their interplay contribute into the mechanism of TDR [13]. However, the DR and re-laminarization at $Re \ll 1$ (described above) occur in channel flows only due to the elastic stress engendered at negligible inertia [9, 11], and they clearly differ from TDR occurring at $Re \gg 1$ [12, 13].

In this Letter we report a key mechanism of DR and re-laminarization at vanishing inertia, observed first in Ref. [9]. We find a good correlation between elastic waves intensity I , wall-normal vorticity fluctuations, and flow resistance in a viscoelastic flow past an obstacle, where I is considered as the key factor in the suggested amplification mechanism by elastic waves. Further, we demonstrate that increasing frequency of elastic waves with Wi results in their strong attenuation that hinders ET growth and leads to DR. We believe that this mechanism is generic to viscoelastic parallel shear flows, in which elastic waves appear.

The experiments are conducted in a straight channel of dimensions $L \times w \times h = 45 \times 2.5 \times 1$ mm³ made of transparent acrylic glass and with an obstacle of $d = 0.3$ mm at its center (Fig. 1(a)). The fluid is driven by N_2 gas at a pressure up to ~ 60 psi and injected at the inlet. As a working fluid, a dilute polymer solution of high molecular weight M_w polyacrylamide ($M_w = 18$ MDa; Polysciences) at a concentration $c = 80$ ppm ($c/c^* \approx 0.4$, where $c^* \approx 200$ ppm is the overlap polymer concentration [14]), is prepared using water-sucrose solvent with sucrose from 25% ($El = 11$) to 65% ($El = 28251$) weight fraction. Due to polymers addition to the solvent, solution viscosity, η , increases about 30%. The solvent viscosity, η_s , is measured by a rheometer (AR-1000; TA Instruments) at 20°C. For $\eta_s = 100$ mPa·s solution, one gets $\lambda = 10 \pm 0.2$ s, obtained by the stress-relaxation method [14]. The latter depends linearly on η_s [14]. The polymer solutions properties for four El are presented in Supplementary Table S1 [15].

High sensitivity ($\pm 0.25\%$ of full scale) differential pressure sensors (HSC series, Honeywell) of different ranges are used to measure the pressure drop ΔP across the obstacle at a separation $L_c = 28$ mm. The exiting fluid is weighed instantaneously $W(t)$ as a function of time by a computer-interfaced balance (BA210S, Sartorius). The time-averaged fluid discharge rate $\bar{Q} = \Delta W / \Delta t$ is used to get the mean velocity $U = \bar{Q} / \rho wh$.

For streak flow visualization and μ PIV measurements via a microscope (Olympus IX70), the solution is seeded with fluorescent particles of diameter $1 \mu\text{m}$ (Fluoresbrite YG, Polysciences). A high-speed camera (FASTCAM Mini WX100, Photron), with a spatial resolution 2048×2048 pixels at a rate of 50 fps is used. The flow in the wake is illuminated by a thin sheet laser (447.5 nm) beam via telescope arrangement. Microscope objectives, 10X for $El = 11$ and 20X for the rest El , are used. For μ PIV measurements, images are acquired with low and high spatial resolutions for temporal velocity power spectra and flow structures, respectively. The FFT based correlation [16] with 32×32 pxl box size corresponding to $18.8 \times 18.8 \mu\text{m}^2$ (at 10X) and $10.6 \times 10.6 \mu\text{m}^2$ (at 20X) and with each box having at least 5 – 10 particles.

A striking difference in the flow dynamics of Newtonian and viscoelastic fluids in the cylinder wake is illustrated via the streak flow images in Fig. 1(b),(c), respectively. For Newtonian fluid in the Stokes limit ($Re = 0.4$), the flow is laminar (Fig. 1(b) left). Above $Re \sim 20$, a boundary layer commences to separate from the cylinder surface leading to a pair of steady eddies attached to the cylinder at $Re \sim 40$, and further to an oscillating vortex pair shown at $Re = 45$ in Fig. 1(b) right.

On the other hand, flow of a viscoelastic fluid exhibits the linear elastic instability at Wi_c and $Re \approx 0.005$. At higher Wi , ET arises [4, 6, 17]. Around ET onset, fluctuating wall-normal vortices are observed in the downstream wake at $Re = 0.011$, $Wi = 312$ for $El = 28251$ (Fig. 1(c) left), contributing to an increase of f/f_{lam} . At $Re \gg 1$, an interplay of inertial and elastic stresses can lead to a suppression of small scale vortices for $El \sim \mathcal{O}(1)$ and thereby to a reduction of the frictional drag [18] leading to the TDR regime [12, 13]. In contrast, in Fig. 1(c) right, the visible suppression of small-scale fluctuating vortices in a viscoelastic flow takes place at $Re = 45$, $Wi = 492$ ($El = 11$), deep in the DR regime that can be compared with the Newtonian case at the same Re (Fig. 1(b) right). In this case, the inertial stress is still significantly smaller than the elastic one, meaning that the DR as well as re-laminarization phenomena are solely governed by the elastic stress.

A detailed demonstration of the flow structures in all three flow regimes: transition, ET, and DR, is presented in Supplementary Fig. S1 [15] at various (Re, Wi, El) . In Supplementary Fig. S1(a), we show evolution of the flow regimes as a function of Re and Wi while keeping $El = 28251$ fixed. At $Wi = 1.83$ and $Wi = 38.6$ (first two images), the flow structure of potential and weakly perturbed laminar flow in the vicinity of the

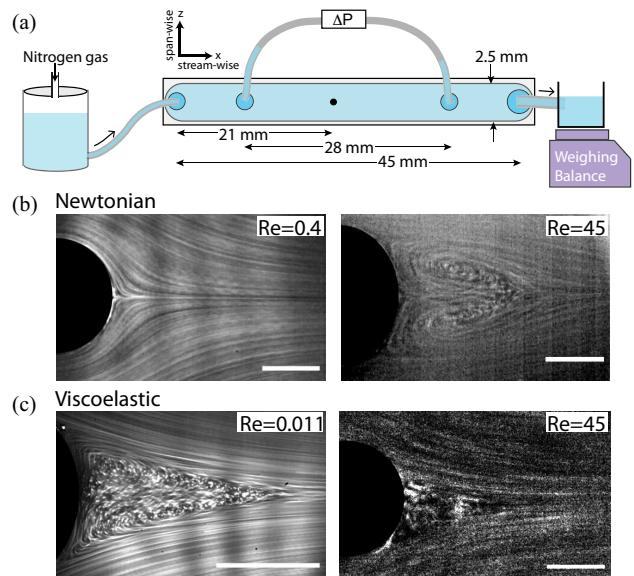


FIG. 1. (a) Schematic of the experimental setup (not to scale). Long-exposure particle streak images of the flow in the wake of the cylinder for (b) Newtonian fluid at $Re = 0.4$ and 45, and (c) viscoelastic fluid at $(Re, Wi, El) = (0.011, 312, 28251)$ and $(45, 492, 11)$. The scale bars are $150 \mu\text{m}$. Flow direction is from left to right.

obstacle are shown, respectively. With a further increase of (Re, Wi) , flow becomes irregular exhibiting ET, which subsequently weakens at higher (Re, Wi) leading to DR [6, 17]. At $El = 28251$, the transition to ET appears at $Wi \sim 360$ (Fig. 1(c)) leading to the growth of fluctuating vorticity, and the vortex dynamics becomes more vigorous up to $Wi = 1050$, at which the ET-DR transition takes place. At further Wi increase, the vortex dynamics slows down and small-scale vortices are progressively suppressed leading to a smoother spatial scale and DR. For instance, the unsteady flow structures are constricted only in the proximity of the wake ($\sim 0.2d$) at $Re = 0.14$ and $Wi = 4035$, contrary to structures spanning up to the obstacle size at $Wi = 312$ (Supplementary Fig. S1(a) [15]).

We perform the measurements of the friction factor as a function of Wi for four El values, calculated as $f = 2\Delta P D_h / \rho L_c U^2$ and normalized by $f_{lam} \sim Re^{-1}$ (see Supplementary Fig. S2 [15]). Here $D_h = 2wh / (w + h) = 1.43$ mm is the hydraulic radius [6]. The elastic transition is evident on a high-resolution plot by the exponent 0.5 in f/f_{lam} versus Wi (Fig. S2). The changes of f/f_{lam} with Wi qualitatively similar for all El : the transition and ET regimes show a drag enhancement, followed by a decrease of f/f_{lam} with increasing Wi , indicating the transition to DR. Further, the scaling exponents of the f/f_{lam} on Wi above the secondary instability (Fig. S2) are approximately the same at all El , i.e. $Wi^{0.2 \pm 0.04}$ and $Wi^{-0.18 \pm 0.05}$ for ET and DR, respectively. The exponent 0.2 in ET is close to the values found in

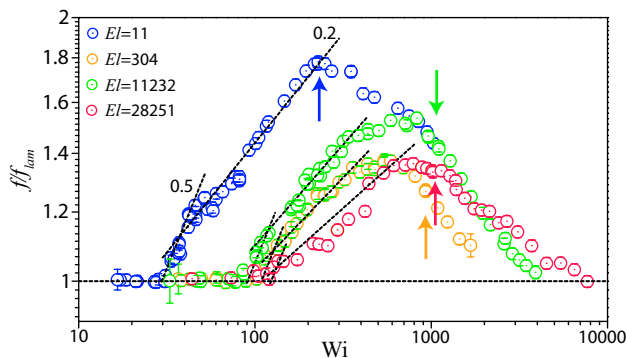


FIG. 2. Normalized friction factor f/f_{lam} versus Wi for four El . Dashed lines are fits with an exponent value of 0.5 and 0.2 in the elastic instability and ET regimes, respectively. Arrows indicate ET to DR transitions.

various configurations of channel flow with and without perturbations [11, 19, 20]. Obviously, the linear elastic instability, ET, and DR occur at different Wi and Re for four El (Fig. S2 and in Supplementary Table S1 [15]). For Newtonian fluid, a drag enhancement begins at $Re \approx 35$ (Supplementary Fig. S2 and Fig. 1(b)). Strikingly, for the high elasticity fluids ($El = 11232$ and 28251), the drag reduction continues until the flow re-laminarizes, i.e. f/f_{lam} returns back to the laminar value at $(Re, Wi) \approx (0.35, 4000)$ and $(0.27, 7627)$, respectively. Moreover, the observations of flow structures via streak images in Supplementary Fig. S1 [15] corroborate well with the dependence of f/f_{lam} on Wi for $El = 28251$ (Fig. S2).

Next, we unravel the role of elastic and inertial stresses in flow structures that lead to a non-monotonic dependence of f/f_{lam} on Wi in Fig. S2. Similarly, the role of inertia in the presence of elastic stress field is explored by varying Re from low to moderate values, while maintaining Wi nearly the constant ($\approx 230 \pm 7\%$), as shown in Supplementary Fig. S1(b) [15]. We achieve this goal for the fluids with different El . In the limit of vanishing Re and $Wi \gg 1$, the elastic Hopf instability occurs in the form of oscillating vortices, as shown at $Wi = 227$ (Supplementary Fig. S1(b), first image), whereas at $Wi \approx 360$, corresponding to ET, fluctuating wall-normal vortices are found. At $Re = 0.02$ and $El = 11232$, the spatial extent of the vortical structure declines and confines narrowly to the obstacle (Supplementary Fig. S1(b), second image). At further increase in $Re = 0.7$ ($El = 304$), the extent of fluctuating vortices expands again in the wake (Supplementary Fig. S1(b), third image). And finally at $Re = 22$ and $El = 11$, the turbulent eddies extent grows filling the expanding downstream wake (Supplementary Fig. S1(b), fourth image). However, the non-monotonic variations in structure dynamics and wake extent, at nearly the same Wi and increasing Re , are predominantly due to the elastic stress, since inertial effects are much less

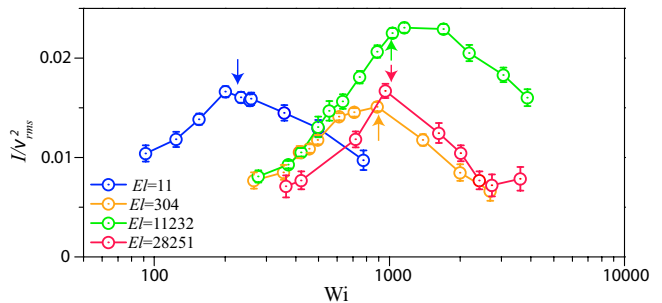


FIG. 3. Normalized intensity of elastic waves (I/v_{rms}^2) versus Wi . Arrows indicate the transition values of Wi from ET to DR, which should be compared with those marked in Fig. S2.

significant.

Elastic waves are non-dispersive with the wave speed depending on stress instead of elasticity of the medium, analogous to the Alfvén wave in plasma [10]. To excite either Alfvén or elastic waves the perturbations should be transverse to the propagation direction. Elastic wave intensity (peak height in velocity spectrum) plays a key role in giving rise to ET and DR [21]. We perform μ PIV measurements of span- and stream-wise velocity field in a wide range of Wi . From the peaks in span-wise velocity spectra shown in lin-log coordinates (see typical spectra for $El = 11232$ in Supplementary Fig. S3 [15]), we obtain the dependence of the normalized elastic wave intensity I/v_{rms}^2 (Fig. S4) and frequency ν_{el} (Fig. 5(a)) on Wi in both ET and DR. Here, v_{rms} is rms fluctuations of span-wise velocity. The dependence of I/v_{rms}^2 on Wi is shown in Fig. S4; I/v_{rms}^2 grows with Wi in the ET regime and decreases in DR for all El and shows power-law behaviour (Supplementary Fig. S4 [15]). To prove correlation between frictional drag and elastic wave intensity, we plot f/f_{lam} (Fig. S2) against I/v_{rms}^2 (Fig. S4) at nearly the same Wi in both ET and DR regimes for all El (Fig. 4(a),(b)). The linear dependence of f/f_{lam} on I/v_{rms}^2 indicates an excellent correlation in the growth of the friction factor and intensity of elastic waves in ET and their decay in DR and re-laminarization. Also, wall-normal vorticity in streak flow images agree well with the observed correlation in both regimes (Fig. 1(b) and Supplementary Fig. S1(a) at $El = 28251$).

Further, we estimate the wave number (k_{el}) of the elastic waves using ν_{el} and the elastic wave speed (c_{el}) given in Ref. [10]; their dependencies on Wi are shown in Fig. 5. The elastic wave frequency ν_{el} grows non-monotonically up to two orders of magnitude with Wi (Fig. 5(a)), however, the wave number k_{el} does not vary substantially, particularly in DR (Fig. 5(b)). Elastic wave intensity and its frequency and wavenumber show reasonable agreement on ET-DR transition Wi values for all El , see Supplementary Fig. S5 [15]. The elastic instability threshold Wi_c , and the onset Wi values for ET and DR at each El are tabulated in Supplementary

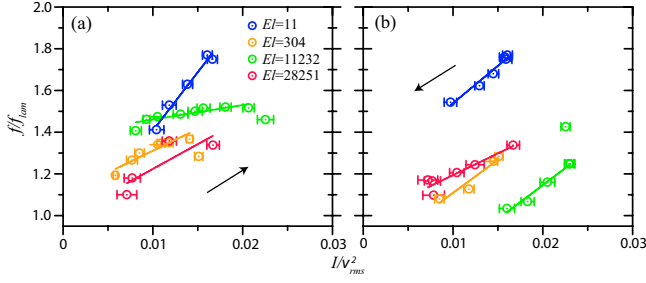


FIG. 4. Correlation between the friction factor and normalized elastic wave intensity in (a) ET and (b) DR regimes for various El . Solid lines are linear fit to the data. Arrows indicate the direction of increasing Wi .

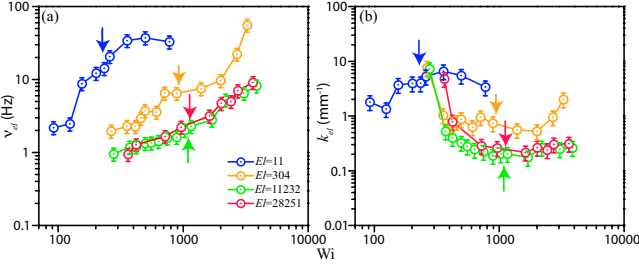


FIG. 5. Dependence of (a) frequency ν_{el} and (b) wave number k_{el} of elastic waves on Wi for different El . Arrows indicate the Wi values of transition from ET to DR.

Table S1 [15].

Similar agreement is observed in two additional analyses: geometrical characterization of the wake (Supplementary Fig. S6), v_{rms}^2 (Supplementary Fig. S7(a)), and the dependence of f/f_{lam} on v_{rms}^2 (Supplementary Fig. S7(b),(c)). We compute both surface area (A) and length (l) of the wake from the streak images as a function of Wi for all values of El . Supplementary Fig. S6 [15] shows normalized area ($4A/\pi d^2$) and length (l/d) of the wake versus $Wi - Wi_c$. Above the instability $Wi > Wi_c$, the wake grows up to the ET-DR transition, resulting in increase of A and l with Wi , whereas beyond the ET-DR transition, both A and l decrease with Wi . In Supplementary Fig. S7 [15], analogous changes in v_{rms}^2 behaviour with Wi are observed. These observations well corroborate with f/f_{lam} (Fig. S2 and Supplementary Fig. S7(b),(c)).

The main observation for understanding the mechanism of the ET attenuation leading to DR and re-laminarization is an excellent correlation between f/f_{lam} and I/v_{rms}^2 (Fig. 4). Indeed, the larger (smaller) f/f_{lam} , the greater (smaller) I/v_{rms}^2 , and I/v_{rms}^2 tends to zero at re-laminarization, quantified in their dependence in Fig. 4. Thus, the observed correlation between the frictional drag and elastic wave intensity suggests the following plausible mechanism of ET suppression resulting in DR and re-laminarization.

Synchronous interaction of the elastic waves with wall-normal vorticity fluctuations leads to their amplification in ET and subsequent suppression in DR. This mechanism of the resonant interaction results in an effective energy pumping from the elastic waves to wall-normal vortices. The physics of the interaction of the elastic waves with fluctuating vortices is analogous to the Landau wave damping [22], occurred due to the resonant interaction of electromagnetic waves with electrons in plasma, when the electron velocity coincides with the wave phase speed. Similarly, acoustic damping occurs in sound-gas bubble interaction [23] resulting in strong wave attenuation. It is also similar to the amplification mechanism of wall-normal fluctuating vortices by the elastic waves in elastically driven Kelvin-Helmholtz-like instability [24]. Then an increase of the wall-normal vorticity results in f/f_{lam} growth at increasing I/v_{rms}^2 in ET and its reduction at diminishing I/v_{rms}^2 in the DR regime.

Then the further question arises: what causes a drastic change from I/v_{rms}^2 growth in ET to its decrease in DR? We suggest that the main reason is the increase in elastic wave dissipation [21] due to increasing ν_{el} . Indeed, there are two plausible mechanisms of the elastic wave attenuation: the elastic stress relaxation limiting the range of elastic wave existence at low k_{el} or low ν_{el} , and viscous dissipation [21] restricting from high k_{el} or high ν_{el} . The former has a scale-independent attenuation, which at low values satisfies the relation $\lambda\omega > 1$, whereas the latter provides low attenuation at high ν_{el} via the inequality $\omega \geq \eta k_{el}^2/\rho$, where $\omega = 2\pi\nu_{el}$. Using both inequalities, one gets the range of low dissipation of the elastic waves, which by substitution $\omega = c_{el}k_{el}$ leads to $\sim 10^{-2} < \nu_{el} < \rho c_{el}^2/2\pi\eta$ at $c_{el} = 0.5 \times 10^{-3}(Wi - Wi_c)^{0.73}$ m/s for $El = 11232$ (similar estimates can be made for other El) [10]. From the second part of the inequality, one finds that the low dissipation range collapses at $Wi_{ET-DR} = 1030$ for f/f_{lam} (Fig. S2) and I/v_{rms}^2 (Fig. S4) occurs at approximately $\nu_{el} \geq 8$ Hz, in a reasonable agreement with the experimental value of ≈ 2 Hz (Fig. 5(a)). Additional damping of elastic wave intensity occurs due to a resonant pumping of energy into the fluctuating vorticity, which is unaccounted in the above estimates. The latter may reduce ν_{el} at which ET-DR transition should take place. This elastic wave damping is analogous to the Landau damping of electromagnetic waves in plasma, as mentioned above [22]. Thus, the collapse of low dissipation range of the elastic waves and so the appearance of large attenuation is the reason for the emergence of the DR regime.

In summary, our experiments suggest the physical origin of the existence of DR and re-laminarization at $Re \ll 1$. The correlation of the frictional drag with elastic wave intensity, and wall-normal vorticity observed in the ET and DR regimes, indicate that the interaction of the elastic waves with fluctuating wall-normal vortices leads to either their amplification or attenuation. Thus, the larger (smaller) elastic wave

intensity, the larger (smaller) the frictional drag, which explains the appearance of DR at $Re \ll 1$.

Acknowledgement. We thank G. Falkovich for discussion and Guy Han for technical support. We are grateful to N. Jha for his help in μ PIV measurements.

This work is partially supported by the grants from Israel Science Foundation (ISF; grant #882/15 and grant #784/19) and Binational USA-Israel Foundation (BSF; grant #2016145).

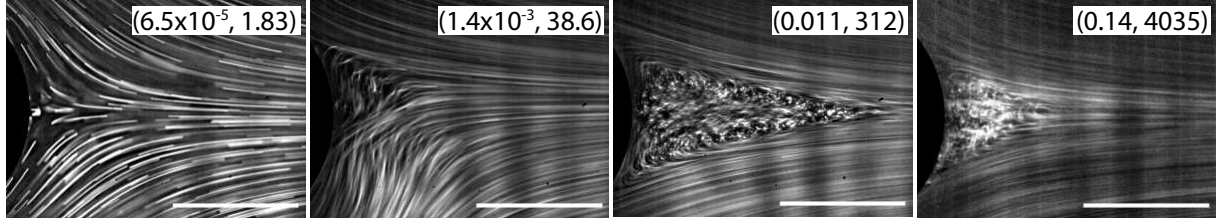
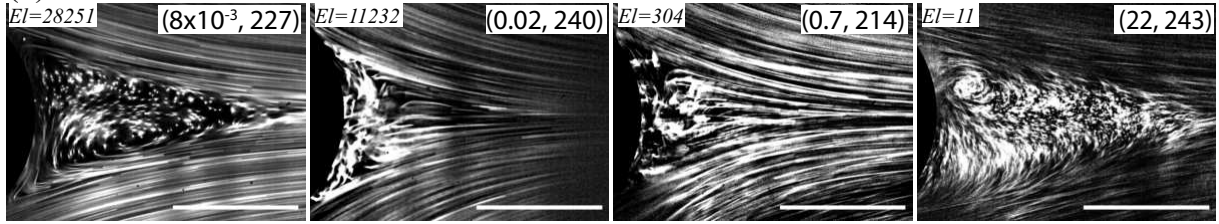
*equal contribution

-
- [1] Steinberg, V. Elastic Turbulence: An Experimental View on Inertialess Random Flow. *Annu. Rev. Fluid Mech.* **53**, 27–58 (2021).
- [2] Groisman, A. and Steinberg, V. Elastic turbulence in a polymer solution flow. *Nature* **405**, 53–55 (2000).
- [3] Larson, R. G. Instabilities in viscoelastic flows. *Rheola Acta* **31**, 213–263 (1992).
- [4] Shaqfeh, E. S. G. Purely Elastic Instabilities in Viscometric Flows. *Annu. Rev. Fluid Mech.* **28**, 129–185 (1996).
- [5] Pakdel, P. and McKinley, G. H. Elastic Instability and Curved Streamlines. *Phys. Rev. Lett.* **77**, 2459–2462 (1996).
- [6] Varshney, A. and Steinberg, V. Elastic wake instabilities in a creeping flow between two obstacles. *Phys. Rev. Fluids* **2**, 051301(R) (2017).
- [7] Bird, R. B. and Hassager, O. *Dynamics of Polymeric Liquids: Fluid Mechanics*, volume 1 & 2. Wiley, New York, (1987).
- [8] Varshney, A. and Steinberg, V. Mixing layer instability and vorticity amplification in a creeping viscoelastic flow. *Phys. Rev. Fluids* **3**, 103303 (2018).
- [9] Varshney, A. and Steinberg, V. Drag enhancement and drag reduction in viscoelastic flow. *Phys. Rev. Fluids* **3**, 103302 (2018).
- [10] Varshney, A. and Steinberg, V. Elastic Alfvén waves in elastic turbulence. *Nat. Commun.* **10**, 652 (2019).
- [11] Jha, N. K. and Steinberg, V. Universal coherent structures of elastic turbulence in straight channel with viscoelastic fluid flow. *arXiv* **2009.12258** (2020).
- [12] Virk, P. S. Drag reduction fundamentals. *AIChE J.* **21**, 625–656 (1975).
- [13] Sreenivasan, K. R. and White, C. M. The onset of drag reduction by dilute polymer additives, and the maximum drag reduction asymptote. *J. Fluid Mech.* **409**, 149–164 (2000).
- [14] Liu, Y., Jun, Y., and Steinberg, V. Concentration dependence of the longest relaxation times of dilute and semi-dilute polymer solutions. *J. Rheol.* **53**, 1069 (2009).
- [15] See Supplemental Material at.
- [16] Thielicke, W. and Stamhuis, E. J. PIVlab – Towards User-friendly, Affordable and Accurate Digital Particle Image Velocimetry in MATLAB. *J. Open Res. Soft.* **2**, p.e30 (2014).
- [17] Grilli, M., Vázquez-Quesada, A., and Ellero, M. Transition to Turbulence and Mixing in a Viscoelastic Fluid Flowing Inside a Channel with a Periodic Array of Cylindrical Obstacles. *Phys. Rev. Lett.* **110**, 174501 (2013).
- [18] Nolan, K. P., Agarwal, A., Lei, S., and Shields, R. Viscoelastic flow in an obstructed microchannel at high Weissenberg number. *Microfluid. Nanofluid.* **20**, 101 (2016).
- [19] Li, Y. and Steinberg, V. Universality in the properties and structures of viscoelastic channel flows with weak and strong perturbations. *arXiv* **2201.06342** (2022).
- [20] Steinberg, V. New direction and perspectives in elastic instability and turbulence in various viscoelastic flow geometries without inertia (short review). *Low Temp. Phys.* **48**, 552–568 (2022).
- [21] Balkovsky, E., Fouxon, A., and Lebedev, V. Turbulence of polymer solutions. *Phys. Rev. E* **64**, 056301 (2001).
- [22] Landau, L. D. On the vibrations of the electronic plasma. *J. Phys. (USSR)* **10**, 25–34 (1946).
- [23] Ryutov, D. D. Analog of Landau damping the problem of sound-wave propagation in a liquid with gas bubbles. *Pis'ma Zh. Eksp. Teor. Fiz.* **22**, 446–449 (1975).
- [24] Jha, N. K. and Steinberg, V. Elastically driven Kelvin-Helmholtz-like instability in straight channel flow. *Proc. Natl. Acad. Sci. USA* **118**, e2105211118 (2021).

TABLE S1. Properties of dilute polymer solutions ($c = 80$ ppm) at various water-sucrose concentrations at 20°C .

Sucrose(wt%)	$\rho(\text{Kg/m}^3)$	$\eta_s(\text{mPa}\cdot\text{s})$	$\eta(\text{mPa}\cdot\text{s})$	$\lambda(\text{s})$	El	Wi_c	ET	$ET - DR$
25	1104	3.3	3.6	0.3	11	30	50	230
47	1215	16.2	20.8	1.6	304	107	260	900
60	1286	100	130	10	11232	96	275	1030
65	1310	165	215	15.5	28251	110	360	1050

SUPPLEMENTAL MATERIAL

(a) constant El (b) constant Wi FIG. S1. Particle streak flow images of the wake at various (Re, Wi) and El . Evolution of flow structures in the wake of the cylinder: (a) at constant $El \sim 28251$ and (b) at nearly constant $Wi \approx 230 \pm 7\%$, and for different Re and El values. The scale bars are $150 \mu\text{m}$. Flow direction is from left to right.

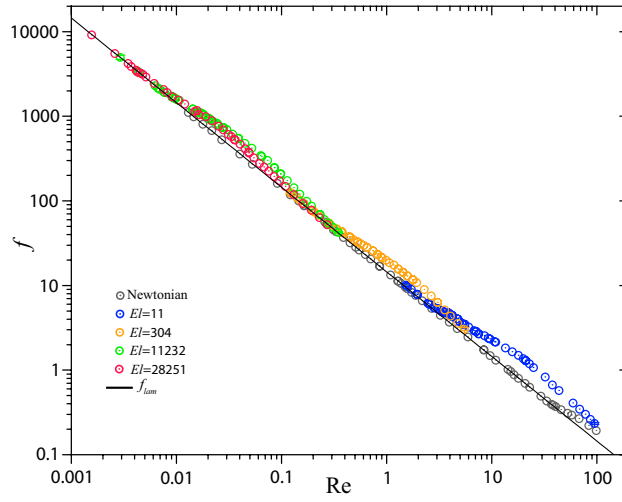


FIG. S2. Friction factor as a function of Re for four values of El and Newtonian solvent. The solid line represents the friction factor for a Newtonian laminar flow, $f_{lam} \sim Re^{-1}$.

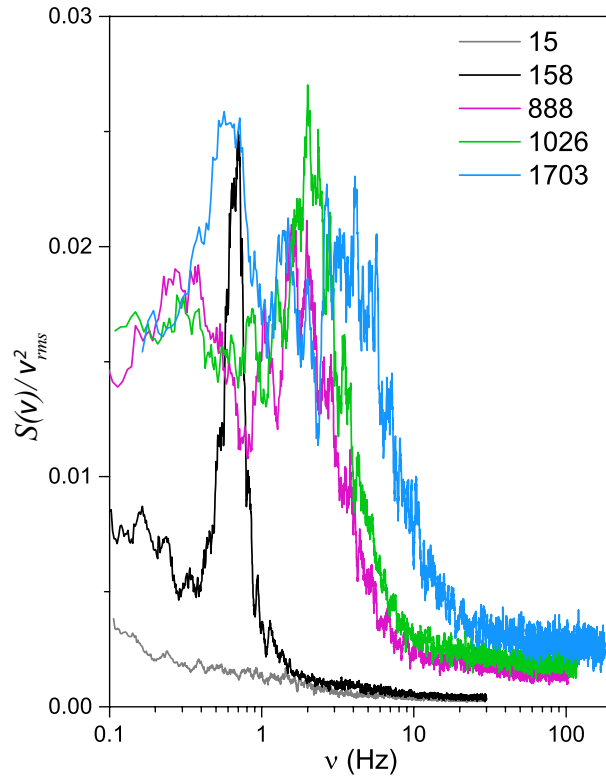


FIG. S3. Normalized span-wise velocity spectra $S(v)/v_{rms}^2$ for $El = 11232$ at different Wi in four flow regimes: laminar at $Wi = 15 < Wi_c$, above the elastic instability exhibiting a sharp peak of the Hopf oscillations, similar to that investigated in a flow between two widely spaced obstacles (Ref. [6] in the main text), ET at $Wi = 888$ and 1026 , and in DR at $Wi = 1703$.

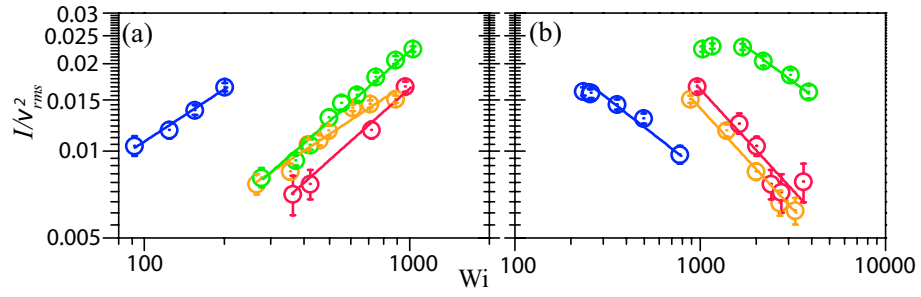


FIG. S4. Normalized intensity of elastic waves (I/v_{rms}^2) versus Wi in log-log scales exhibiting power-law behavior in (a) ET and (b) DR.

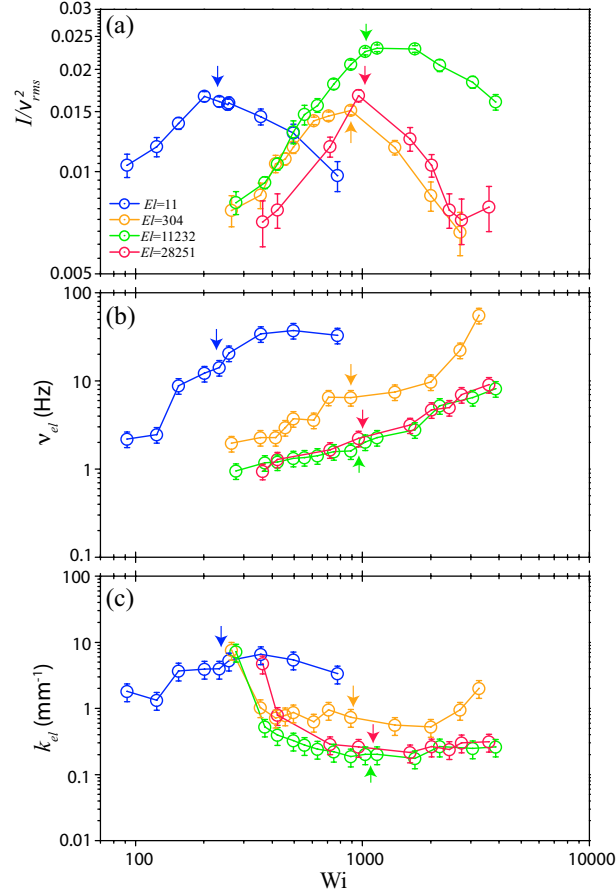


FIG. S5. Dependence of (a) intensity I/v_{rms}^2 , (b) frequency ν_{el} , and (c) wave number k_{el} of elastic waves on Wi for different El . Arrows indicate the Wi values of transition from ET to DR.

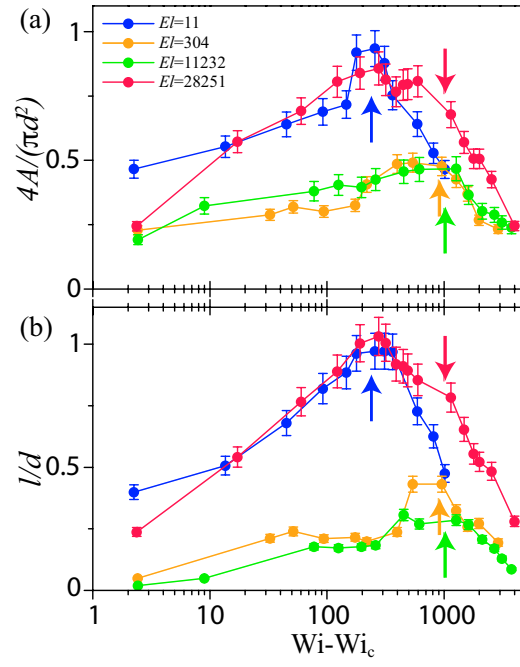


FIG. S6. Surface area and length of downstream wake structures with Wi . Variation of (a) normalized wake area ($4A/\pi d^2$) and (b) normalized wake length (l/d) with $Wi - Wi_c$ for different El . Arrows indicate the transition values of Wi from ET to DR.

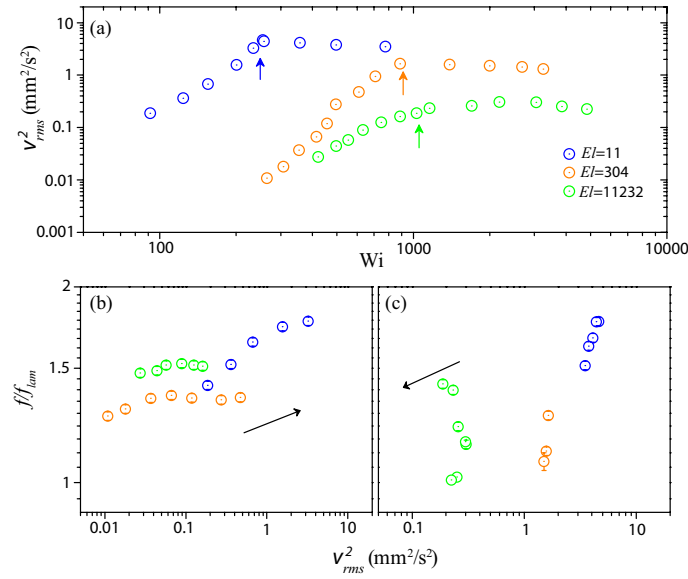


FIG. S7. (a) Square of rms fluctuations of span-wise velocity, v_{rms}^2 , as a function of Wi . Arrows in (a) indicate the transition values of Wi from ET to DR. Dependence of f/f_{lam} on v_{rms}^2 in (b) ET and (c) DR regimes. Arrows in (b) and (c) indicate direction of increasing Wi .